Strong-field tunneling ionization in the relativistic regime

Xiaoyang Yu[1] and Yunquan Liu[1,2,3,4,*]

[1]*State Key Laboratory for Mesoscopic Physics and Collaborative Innovation Center of Quantum Matter,*
School of Physics, Peking University, Beijing 100871, China
[2]*Center for Applied Physics and Technology, HEDPS, Peking University, Beijing 100871, China*
[3]*Collaborative Innovation Center of Extreme Optics, Shanxi University, Taiyuan, Shanxi 030006, China*
[4]*Beijing Academy of Quantum Information Sciences, Haidian, Beijing 100193, China*

We study the photoelectron energy and momentum distributions of strong-field tunneling ionization in the relativistic regime. Using the relativistic strong-field approximation, we have derived the position of the tunnel exit, the initial momentum distributions at the tunnel exit, and the instantaneous ionization rate when the electron tunnels through the Coulomb barrier in the relativistic regime. Since the tunneling electron energy is of the order of 1% of the rest of its mass, those nonadiabatic tunneling coordinates are quite different from the nonrelativistic case. We further incorporate the nonadiabatic relativistic tunneling coordinates into the classical trajectory Monte Carlo model and have calculated photoelectron energy and momentum distributions by accurately considering the field distribution in the focus of relativistic femtosecond laser pulses. We show that the nonadiabatic tunneling effect and the focal field distribution are very crucial to modeling strong-field ionization in the relativistic regime because the quiver radius of electrons can be as large as the beam waist.

I. INTRODUCTION

With the invention of chirp pulse amplification (CPA) [1], the peak intensity of a femtosecond laser can now be higher than 10^{22} W/cm^2 [2]. With that, strong-field ionization of highly charged ions in the relativistic regime becomes of great interest [3–7]. The strong-field approximation (SFA) [8] has been developed for strong-field ionization in the relativistic regime [9,10]. The standard SFA neglects the influence of the Coulomb field by using the Volkov wave function to describe the electron dynamics in the continuum [11]. However, this approximation is not valid for strong-field ionization of highly charged ions in ultraintense laser fields. The total ionization rate has been obtained by using the Wentzel-Kramers-Brillouin (WKB) approximation [12–14]. The eikonal-Volkov wave function has been proposed to take the place of the Volkov wave function to correct SFA [15–18]. The nondipole effect for strong-field ionization has also become of great interest [19,20]. Recently, the Coulomb-corrected SFA in the relativistic regime based on the Dirac equation was proposed [21], in which the nonrelativistic effect has been considered [22]. On the other hand, high-order-harmonic generation (HHG) [23] in the relativistic regime is also very interesting for strong-field ionization because it could produce high-energy photons [24,25] with attosecond or zeptosecond pulse duration [26–39]. In theory, the cutoff energy of HHG in the relativistic regime was studied recently [40].

What has remained elusive is to quantitatively describe strong-field ionization and to calculate the photoelectron momentum and energy distributions in the relativistic regime. Particularly, as known, in the relativistic regime the electrons

can quiver as large as the radius of focus. It is very necessary to consider the focal field effect for ultraintense femtosecond laser pulses. In this paper, we develop the quantitative theory to study the photoelectron momentum and energy distributions for strong-field tunneling ionization of highly charged ions in the relativistic regime. We derive the initial momentum distributions at the tunnel exit by considering the nonadiabatic tunneling effect. Incorporating the nonadiabatic tunneling coordinates, we solved the relativistic dynamic equation with consideration of the Coulomb potential. We have calculated the photoelectron angular distributions and energy spectrum for strong-field tunneling ionization by full consideration of the temporal and spatial effect of the relativistic focused femtosecond laser pulses in the relativistic regime.

II. METHOD

A. Relativistic SFA model

We start with the time-dependent Dirac equation to describe the process of the ionization of the highly charged ions by a superstrong linearly polarized laser pulse in the relativistic regime [21],

$$\left(i\gamma^\mu \partial_\mu + \frac{1}{c}\gamma^\mu A_\mu - \gamma^0 \frac{V^{(c)}}{c} - c \right)\psi = 0, \qquad (1)$$

where γ^μ are the Dirac matrices and A_μ is the four-vector of the laser field. $V^{(c)} = -\frac{Z}{r}$ is the Coulomb potential of the atomic core, and the effective nuclear charge Z is determined by the bound state energy via $c^2 - I_p = \sqrt{c^4 - c^2 Z^2}$, where I_p is the ionization potential. In our simulation, we take the highly charged ions with ionization potential $I_p = 3000$ a.u. (atomic units are used throughout the paper unless specified) at the intensity of $I = 1 \times 10^{19}$ W/cm^2 at the wavelength of

*yunquan.liu@pku.edu.cn

800 nm. The phase of the laser pulse no longer only depends on the t, and therefore one should replace t with $\eta = t - \frac{z}{c}$. The electromagnetic field of a plane wave can be written as $\mathbf{E}(\eta) = -E_0 \cos(\omega\eta)\mathbf{e_x}$, $\mathbf{B}(\eta) = -\frac{E_0}{c}\cos(\omega\eta)\mathbf{e_y}$, and $\mathbf{A}(\eta) = \frac{E_0}{\omega}\sin(\omega\eta)\mathbf{e_x}$, where ω is the field frequency and E_0 is the laser field amplitude. The electric field is polarized along the x axis, and the magnetic field is polarized along the y axis. The propagation direction of the laser pulse is along the z axis. Within SFA in the relativistic regime, the transition amplitude can be written as $M(\mathbf{p}) \propto -i \int_{-\infty}^{\infty} d\eta < \mathbf{p}|H_{\text{int}}|\varphi_0(\eta) > \exp[-iS(\eta)]$, where $\mathbf{p}$ is the canonical momentum, $H_{\text{int}} = \gamma^0\gamma^\mu A_\mu$ is the interaction Hamiltonian between laser field and atoms, and φ_0 is the wave function of the ground state of the highly charged hydrogenlike ions. The relativistic kinetic energy is $\varepsilon(\eta) = \varepsilon_0 + \frac{[\mathbf{p}+\mathbf{A}(\eta)/2]\cdot\mathbf{A}(\eta)}{\Lambda}$, where Λ is the constant of motion $\Lambda = \frac{\varepsilon_0 - p_z c}{c^2}$ and $\varepsilon_0 = \sqrt{c^4 + c^2\mathbf{p^2}}$. The action in the tunneling ionization process is expressed as

$S(\eta) = \int_\eta^\infty d\eta'\{\varepsilon_0 - c^2 + I_p + \frac{[\mathbf{p}+\mathbf{A}(\eta')/2]\cdot\mathbf{A}(\eta')}{\Lambda}\}$. For a certain canonical momentum $\mathbf{p}$, we can obtain the saddle points per cycle of the laser field as

$$\omega\eta_1 = \arcsin\left[-\frac{p_x}{E_0/\omega} + i\sqrt{\frac{2\Lambda(\varepsilon - c^2 + I_p) - p_x^2}{(E_0/\omega)^2}}\right],$$

$$\omega\eta_2 = \pi - \arcsin\left[-\frac{p_x}{E_0/\omega} - i\sqrt{\frac{2\Lambda(\varepsilon - c^2 + I_p) - p_x^2}{(E_0/\omega)^2}}\right].$$

$$(2)$$

For each saddle point, the $\eta_s = \eta_r + \eta_i$ can be divided into the real and imaginary parts. Then, within imaginary time theory the tunneling ionization rate of the highly charged hydrogenlike ions is related with the imaginary part and is given by

$$W \propto \exp[2\text{Im}S] = \exp\left[2\left(c^2 - \varepsilon - I_p - \frac{E_0^2}{4\Lambda\omega^2}\right)\eta_i + \frac{E_0^2 \sinh(2\omega\eta_i)\cos(2\omega\eta_r)}{4\Lambda\omega^3} - \frac{2E_0 p_x \sinh(\omega\eta_i)\sin(\omega\eta_r)}{\Lambda\omega^2}\right]. \quad (3)$$

The initial momentum distributions at the tunnel exit is calculated via back propagation, which is similar with the nonrelativistic case [41]. The momentum $\mathbf{P}(\eta_r)$ at the tunnel exit related to the canonical momentum $\mathbf{p}$ is given by $\mathbf{P}(\eta) = $

$\mathbf{p} + \mathbf{A}(\eta) + \frac{[\mathbf{p}+\mathbf{A}(\eta)/2]\cdot\mathbf{A}(\eta)}{c\Lambda}\mathbf{z}$. The part along the propagation direction $\frac{[\mathbf{p}+\mathbf{A}(\eta)/2]\cdot\mathbf{A}(\eta)}{c\Lambda}\mathbf{z}$ results from the magnetic dipole effect and the mass shift effect. The tunnel exit position can be calculated from the trajectory in the sub-Coulomb-barrier
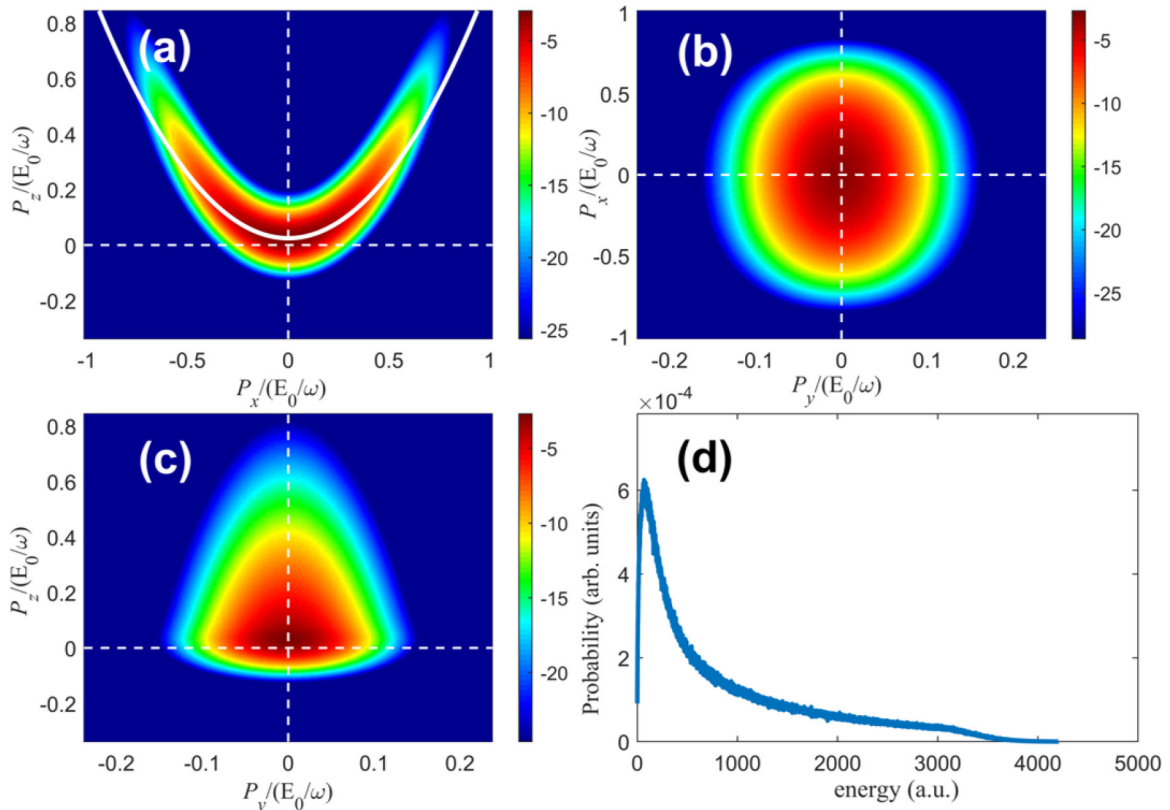

FIG. 1. Photoelectron momentum distributions at the virtual detector calculated by the relativistic SFA in the x-z-plane (a), y-x-plane (b), and y-z-plane (c), respectively. The white curve shows the maximum of the momentum distribution. (d) The energy spectrum of the photoelectron at the detector calculated by the relativistic SFA.
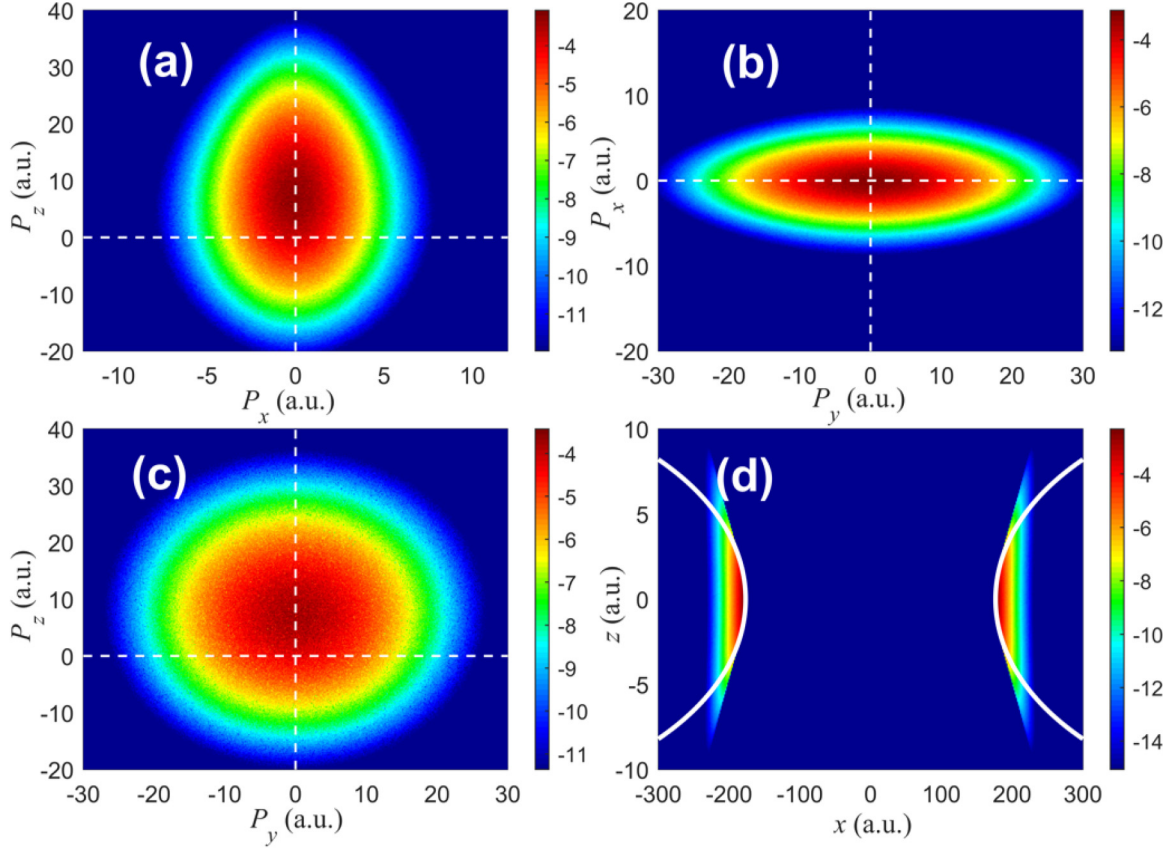
FIG. 2. Photoelectron momentum distribution at the tunnel exit calculated by the relativistic SFA in the x-z-plane (a), y-x-plane (b), and y-z-plane (c), respectively. (d) The position distribution of the photoelectron at the tunneling exit. The white curve shows the position of the tunnel exit predicted by the relativistic PPT theory [13].

using the equation of $\mathrm{Re}[\mathbf{r}(\eta_r)] = \mathrm{Re}[\mathbf{r_0} + \int_{\eta_s}^{\eta_r} d\eta' \mathbf{P}(\eta')/\Lambda]$, where $\mathbf{r_0} = 0$ corresponds to the initial position of the bound electrons. The tunnel exit can also be predicted by the relativistic Perelomov-Popov-Terent'ev (PPT) theory [13], as given by

$$x = \frac{ip_\perp}{eE_g}(\arcsin \tau_0 - \arcsin \tau), \quad y = 0,$$

$$z = \frac{M}{eE_g}\left(\sqrt{1 - \tau^2} - \sqrt{1 - \tau_0^2}\right), \tag{4}$$

where $p_\perp$ is the transverse momentum of the ionization electron. Here $\tau = ieE_g t/M$ and $M = \sqrt{m^2 + p_\perp^2}$. E_g is associated with the bound state energy and τ_0 is related to the imaginary time of the bound state.

B. Relativistic CTMC model

The SFA itself does not fully include the real movement of photoelectrons in the combined relativistic laser field and the Coulomb field. The real trajectories of the electrons in the relativistic laser field would be more complicated since they are the integration of the velocity over time t. Because of the relativistic effect, the electrons do not simply follow the vector of the laser field, as described in the standard SFA. Therefore, there is no analytic expression of the momentum and position of the photoelectrons on the detector in the relativistic

laser field. To do this, we have developed the nonadiabatic relativistic classical trajectory Monte Carlo (CTMC) model. We first sample the initial nonadiabatic coordinates of all of the tunneling electrons at the tunnel exit. The velocity of the relativistic electron associated with the momentum is given by $\mathbf{v} = \frac{c\mathbf{p}}{\sqrt{\mathbf{p}^2 + c^2}}$. After the tunneling, the electron motion in the combined laser and Coulomb fields is governed by the relativistic Newtonian equation,

$$\frac{d}{dt}\left[\frac{\mathbf{v}}{\left(1 - \frac{\mathbf{v}^2}{c^2}\right)^{1/2}}\right] = -\mathbf{E} - \frac{\mathbf{v} \times \mathbf{B}}{c} - \frac{Z\mathbf{r}}{|\mathbf{r}|^3}. \tag{5}$$

III. RESULTS AND DISCUSSION

Firstly, we have calculated the photoelectron momentum distribution using the relativistic SFA. As seen in Figs. 1(a) and 1(c), it reveals a shift of the global maximum of the asymptotic momentum distribution along the laser propagation direction, and, especially, it reveals a parabolic wings structure in the x-z plane. From Eq. (3), one can determine the maximum of the momentum distribution, which is located at a parabolic line along $p_z = I_p/3c + p_x^2/2c(1 + I_p/3c^2)$ while $p_y = 0$ [the white curve in Fig. 1(a)]. In the nonrelativistic limit, the shift will disappear due to the order of $1/c$ [41]. As shown in Fig. 1(b), the final photoelectron momentum distribution calculated by the relativistic SFA reveals a
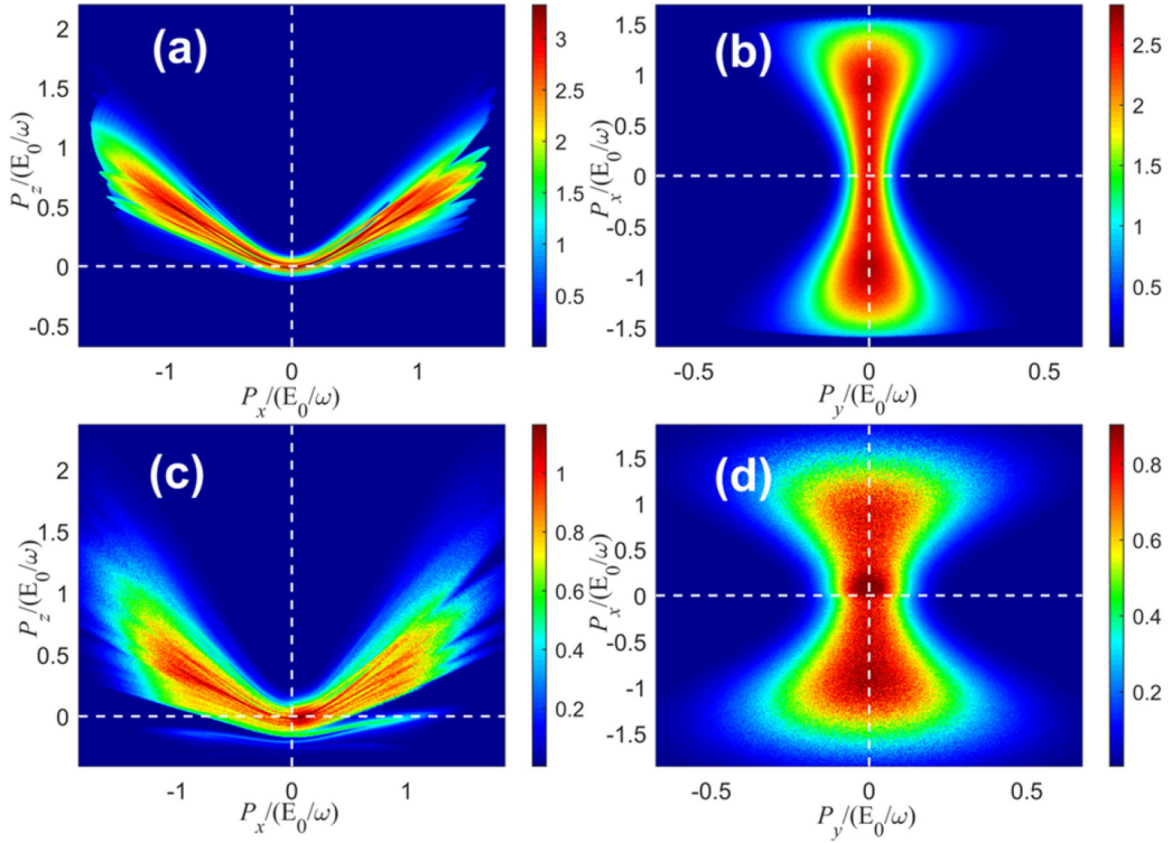
FIG. 3. Photoelectron momentum distribution in the x-z-plane (a),(c), and y-x-plane (b),(d), calculated with the CTMC model in a plane laser field, respectively. In (a),(b), we use the nonadiabatic tunneling coordinates. In (c),(d), we use the adiabatic tunneling coordinates given by ADK theory.

centrosymmetric image in the polarization plane. The energy spectrum of the photoelectron is shown in Fig. 1(d). The photoelectrons with energy 100 a.u. have the maximum probability. The cutoff energy of the photoelectron is around 3500 a.u., which is much lower than $2U_p = 4.3828 \times 10^4$ a.u. as predicted by SFA in the nonrelativistic regime [42].

As shown in Figs. 2(a) and 2(c), the initial momentum distributions at the tunnel exit have an evident shift in the propagation direction. Comparing Fig. 1(a) with Fig. 2(a), we can understand that the shift of the maximum momentum distribution is directly connected with the sub-Coulomb-barrier tunneling. The initial momentum distributions at the tunnel exit reveal a Gaussian distribution in the polarization plane, as shown in Fig 2(b). The tunnel exit position can be calculated from the sub-Coulomb-barrier trajectory with the equation of $\mathrm{Re}[\mathbf{r}(\eta_r)] = \mathrm{Re}[\mathbf{r_0} + \int_{\eta_s}^{\eta_r} d\eta' \mathbf{P}(\eta')/\Lambda]$, where $\mathbf{r_0} = 0$ corresponds to the initial position of the bound electrons, as showed in Fig. 2(d). The $x > 0$ and $x < 0$ parts derive from the different half period per cycle of the laser field. For the high ionization potential, the tunneling exit is very far away from the parent ion in the polarized direction in the relativistic regime. The nonadiabatic relativistic results agree well with the PPT model [13].

Experimentally, in order to obtain extremely high intensity, the beam of the femtosecond laser pulses is always focused tightly. In the relativistic regime, the photoelectron can be accelerated to the same order speed of light within one cycle

of the laser pulse and the photoelectron will move far away from the parent ion. Thus, the temporal and spatial distributions of the tightly focused ultraintense femtosecond laser pulses have a non-negligible influence on the photoelectron movement. We show the calculated photoelectron momentum distributions using the nonadiabatic tunneling coordinates in a plane wave in Figs. 3(a) and 3(b). In the simulation, we take the pulse duration with a trapezoidal envelope comprising a five-cycle flat top and a one-cycle turning on and turning off at 800 nm at the intensity of 1×10^{19} W/cm^2. In Fig. 3(a) the momentum distribution reveals a wing structure in the x-z plane because the photoelectron is oscillating in the x-z plane by the un-neglectable Lorentz force. The momentum distribution of the photoelectron reveals the dumbbell shape in the y-x plane, as shown in Fig. 3(b). The momentum has a wider distribution in the electric-field direction compared with the result of relativistic SFA in Fig. 1. We show the calculated momentum distribution using the adiabatic model in Figs. 3(c) and 3(d). The initial coordinate is given by relativistic Ammosov-Delone-Krainov (ADK) theory [43] and the tunnel exit is derived from the Laudau effective potential theory [44]. There is no initial momentum shift in the propagation direction at the tunnel exit. If comparing the adiabatic results with the nonadiabatic results, one can find that the final momentum distribution using the adiabatic approach is largely extended in the propagation and is shrunken in the electric-field direction.
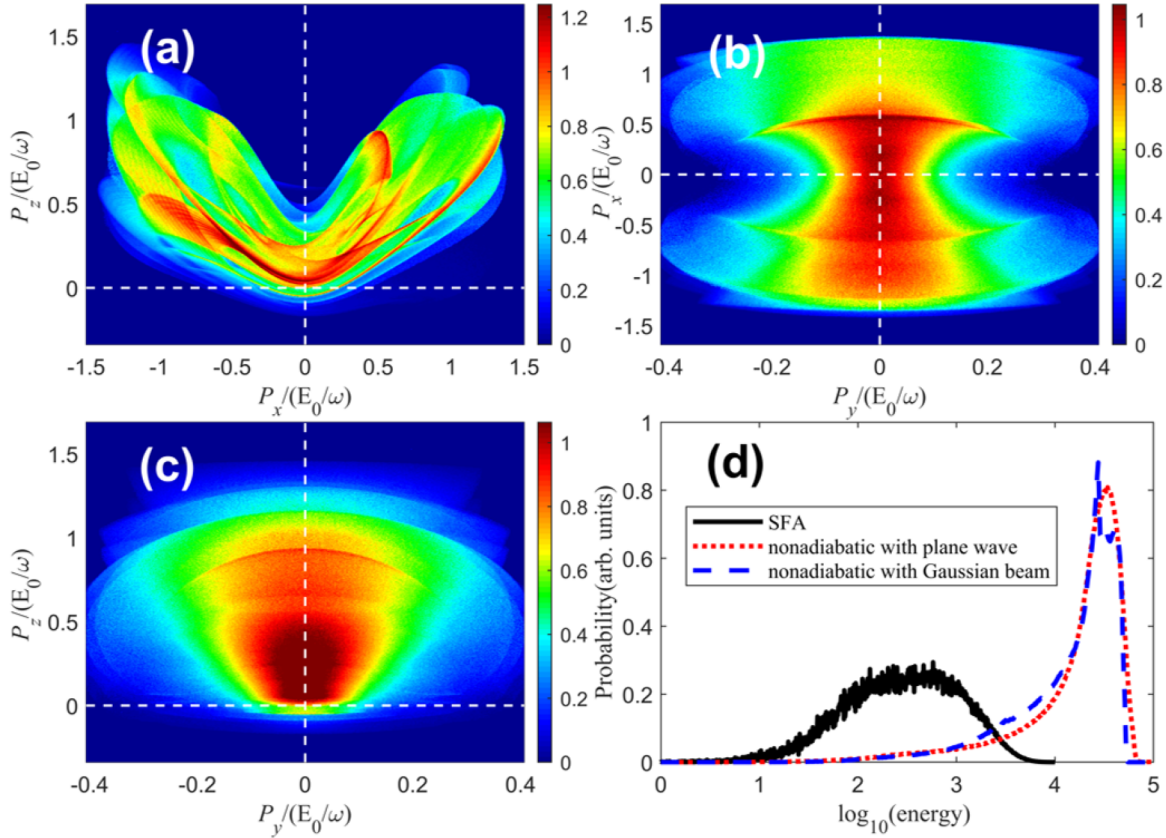
FIG. 4. Photoelectron momentum distribution in the x-z-plane (a), y-x-plane (b), and y-z-plane (c), with the CTMC model in a tightly focused Gaussian beam, respectively. (d) The photoelectron energy spectra calculated by the relativistic SFA (black line), the nonadiabatic CTMC with a plane wave (dotted red line), and with the tightly focused Gaussian beam (dashed blue line).

However, since the electrons can quiver as large as the beam waist, it is necessary to consider the focusing effect of ultraintense femtosecond laser pulses [45]. Since the spatial envelope is ignored if using a plane wave, we then calculated the photoelectron momentum in a tightly focused femtosecond laser pulse in Fig. 4. It is very necessary to include an accurate treatment of E and B field components in the z direction. Here, we assume the radius of the beam waist is 1 μm and the other laser parameters are the same as in Fig. 3. The photoelectron momentum in a tightly focused pulse has wider distribution in the propagation direction than that in a plane wave, as shown in Fig. 4(a). Correspondingly, the photoelectron momentum in a tightly focused pulse along the electric-field direction is much narrower than that in a plane wave, as shown in Fig. 4(b). Because of the tight focusing effect, the high-order electric-field component along the propagation direction will accelerate the electrons forward and the high-order magnetic-field component along the propagation direction will modify the electron motion along the polarization plane. In the y direction, the Coulomb force is more effective. However, the distance between the photoelectron and the parent ion is much larger in the relativistic regime. The velocity of the photoelectron along the y direction changes a little, but the momentum along the y direction has considerable change due to the mass shift. Because the mass shift and Coulomb effect are more isotropic, the final momentum distribution reveals a symmetrical structure along

the y direction, as seen in Fig. 4(c). In the other two directions, there is no full symmetrical pattern. We also calculated the photoelectron energy spectra using the nonadiabatic model in Fig. 4(d); the cutoff energy using the plane wave (dotted red line) is around 6×10^4 a.u. $\sim (2.7U_p)$ and the cutoff energy using the Gaussian beam (dashed blue line) is around 5.5×10^4 a.u. $\sim (2.5U_p)$, which are much lower than $10U_p$ as that in the nonrelativistic regime [46]. The results calculated by the relativistic SFA are also shown in Fig. 4(d) as the black line.

Comparing with the results of the nonadiabatic CTMC model with the relativistic SFA, one can find that the cutoff energy of the photoelectron is much higher and the photoelectron momentum distribution is also extended. This will certainly have a crucial effect on HHG because the Lorentz force due to the laser magnetic field can significantly reduce the returning probability. We use the model to calculate the limit of the cutoff energy of recollision. We define the recollision if the tunnel-ionized photoelectron can move as close to the tunnel exit as expected by the relativistic model, $|\mathbf{r}(t_{re})| = |\mathbf{r}(t_0)|$, where t_{re} is the recollision time of the photoelectron and t_0 is the ionization time of the photoelectron. In Fig. 5(a), we show the probability and energy of returning electrons with respect to the ionization instant. One can see that some of the photoelectrons released after the peak of the laser field can revisit the parent ions. The time window for returning using the nonadiabatic coordinates ranges from 4.9° to 19°,
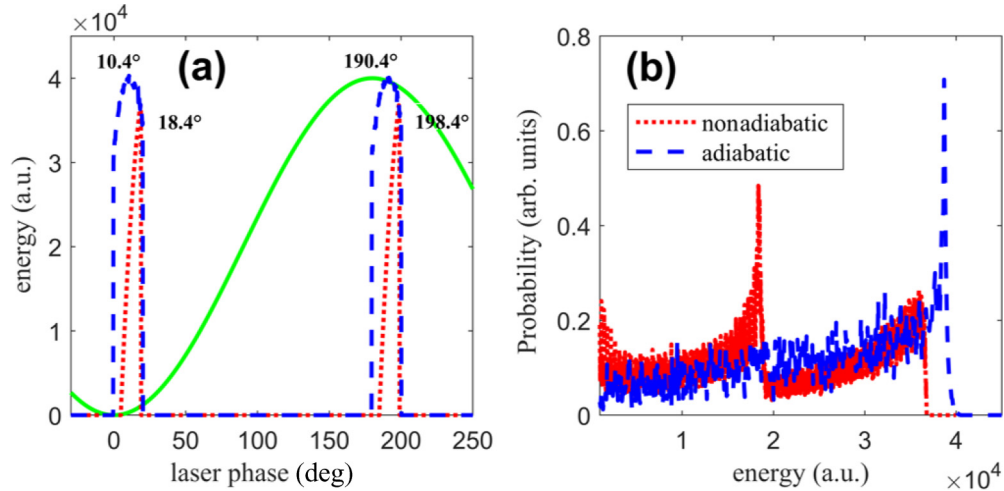
FIG. 5. (a) The returning photoelectron energy with respect to the ionization time calculated with the adiabatic (dashed blue line) and nonadiabatic (dotted red line) model. The green curve shows the laser field. (b) The returning probability with respect to the electron energy within one laser cycle calculated with the adiabatic (dashed blue line) and nonadiabatic (dotted red line) model.

which is much narrower than the nonrelativistic case [39]. The time window using the adiabatic tunneling coordinates ranges from 0° to 20°, which is broader than that in the nonadiabatic case. In Fig. 5(b), the maximum energy of return adiabatic electrons (dashed blue line) is about 4×10^4 a.u., $\sim(1.82U_p)$; they are released at the phase of 10.4° and 190.4°.

The maximum energy of return nonadiabatic electrons (dotted red line) is about 3.7×10^4 a.u., $\sim(1.8U_p)$; they are released at the phase of 18.4° and 198.4°. The electrons with the return energy 1.8×10^4 a.u. have the maximum returning probability, which are released at the phase of 10° because of the nonadiabatic effect. The return energy of the photoelectron
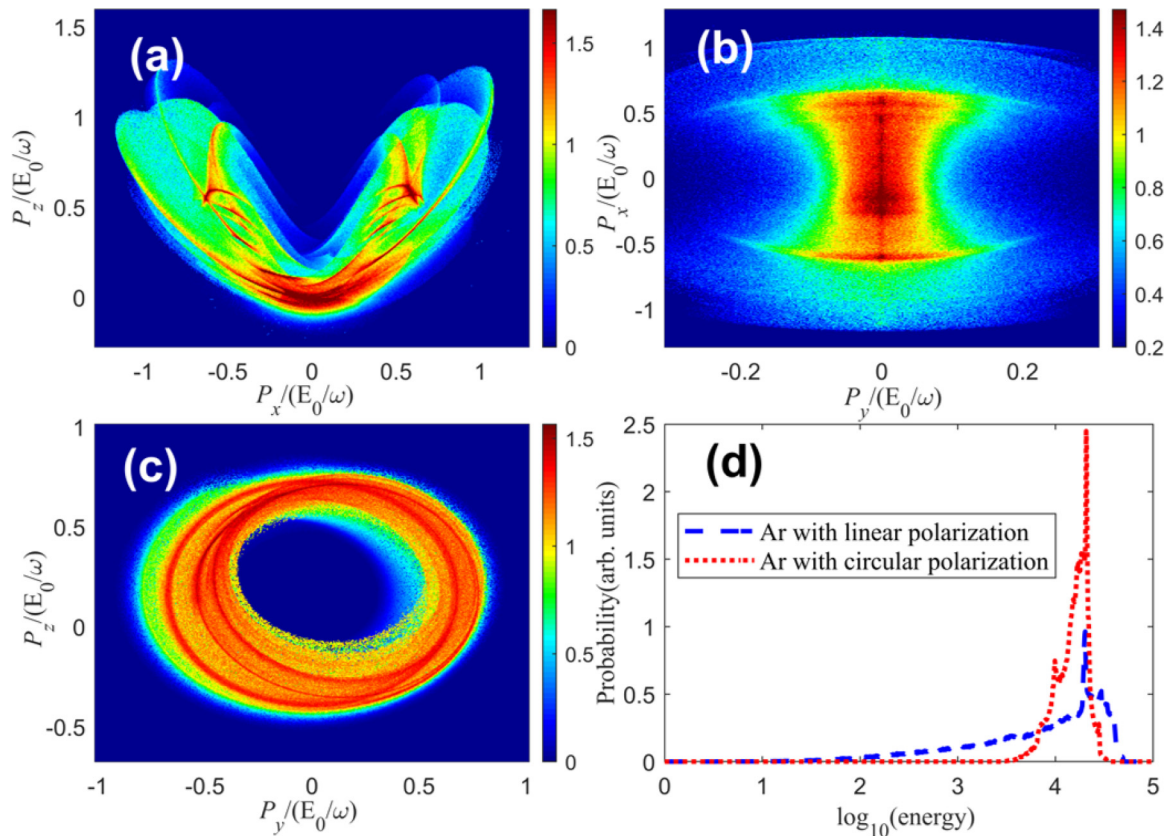

FIG. 6. The calculated photoelectron momentum distribution of Ar in the x-z plane (a), and x-y plane (b), in the tightly focused laser pulse with linear polarization. Photoelectron momentum distribution of Ar in the x-y plane (c) in the tightly focused laser pulse with circular polarization. (d). The energy spectrum of the photoelectron in linear polarization (dashed blue line) and circular polarization (dotted red line).
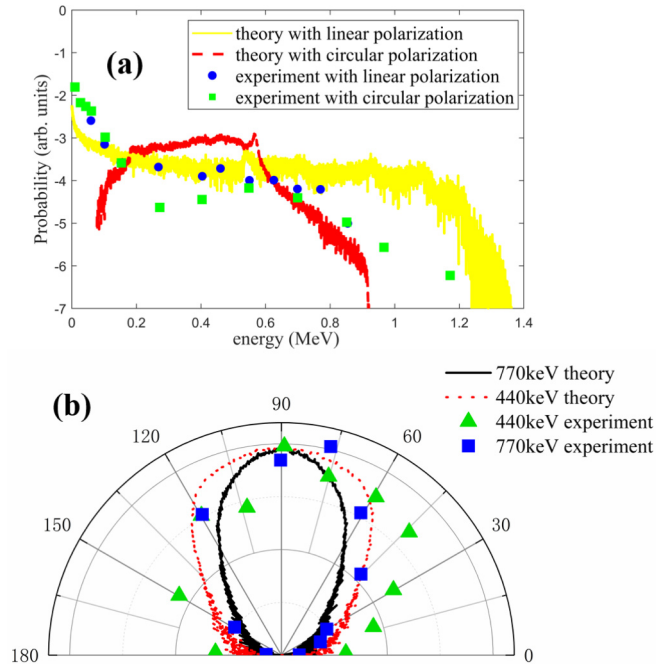
FIG. 7. (a) The photoelectron energy spectrum of Ar atoms calculated by the nonadiabatic CTMC with linear polarization (yellow line) and circular polarization (dotted red line). The measurement of the photoelectron energy spectrum of Ar atoms in Ref. [3], with linear polarization (blue circles) and circular polarization (green squares). (b) The angular distributions in the polarization plane are measured in Ref. [3] with the energy of 400 keV (green triangles) and 770 keV (blue squares). Calculated results for the energy of 400 keV (dotted red line) and 770 keV (black line).

significantly decreases and it cannot reach the $3.17U_p$ cutoff limit in the nonrelativistic regime [42].

IV. COMPARISON WITH THE EXPERIMENT

To further verify the nonadiabatic model, we have compared the theoretical calculation with the experimental results for the realistic atoms in the relativistic regime [3]. Using similar laser parameters as in the experiments, we have calculated the momentum distribution and energy spectrum of the photoelectron at the detector in a tightly focused femtosecond laser pulse with a trapezoidal envelope comprising of a five-cycle flat top and a one-cycle turning on and turning off at 800 nm at the intensity of 1×10^{19} W/cm^2. We have calculated the results of Ar^{16+} using linear polarization and circular polarization.

We show the momentum angular distribution of the photoelectron with ultraintense linear polarization in Figs. 6(a) and 6(b). The momentum distribution is still oscillating in the x-z plane and the momentum distribution is spatially anisotropic in the polarization plane with electrons more likely to distribute along the electric-field direction as the energy is increased. The model can be extended to strong-field tunneling ionization in the relativistic regime for circular polarization. Similarly, we can derive the nonadiabatic momentum and position distributions at the tunnel exit

based on the relativistic SFA, and the electrons are driven by the circular polarization laser field with the relativistic Newtown equation. The calculated final momentum distribution in the polarization plane is shown in Fig. 6(c). As seen in Fig. 6(d), the cutoff of the photoelectron energy is around 1.24 MeV for the linear polarization. The maximum energy of the photoelectron is around 0.92 MeV for the circular polarization.

The most direct way is to compare the results with the measurement [3]. The experimental and calculated photoelectron energy spectrum are shown in Fig. 7(a). For the linear polarization laser field, the theoretical result agrees well with the experimental results when the energy is lower than 0.8 MeV. The theoretical result has a lager cutoff energy, $\sim$1.24 MeV, than that of the experiment, $\sim$0.8 MeV. For the circular polarization laser field, the theoretical result shows that many more electrons are distributed in the low-energy part. The difference results from the fact that we only obtain the tunneling ionization for the hydrogenlike ion in the theoretic calculation and the photoelectrons from different shells have been measured in the experiment. The theoretic result has a lower cutoff energy, $\sim$0.94 MeV, than the experiment, $\sim$1.2 MeV. We also compare the angular distribution in the polarization plane between the experimental measurement and theoretical calculation in Fig. 7(b). Generally, the theoretical calculation shows good agreement with the experimental measurement.

V. CONCLUSION

In conclusion, we have presented a model to describe strong-field ionization in the relativistic regime. Considering the nonadiabatic effect, we have derived the ionization probability, the position distribution of the tunnel exit, and the initial momentum distributions of photoelectrons at the tunnel exit using the relativistic SFA with the saddle-point approximation. We have further considered the temporal and spatial field distribution of the focused ultraintense femtosecond pulses, and have calculated the photoelectron energy and photoelectron momentum distribution on the basis of the relativistic dynamic movement equation. The precise relativistic model describes a distinct picture of strong-field ionization in the relativistic regime. We show the nonadiabatic tunneling effects, and the focal field distribution are very crucial for the final photoelectron momentum distribution and energy spectrum. The results show that the photoelectron cutoff energy is around $2 - 3U_p$ and is much less than $10U_p$ because of significant reducing of the rescattering probability. We have also discussed the rescattering limit in the relativistic regime. The atomic orbital could also be considered in this relativistic model [47] in the future. Since it is hard to calculate the exact solution of time-dependent Dirac equation nowadays, our approach has provided a way to quantitatively model strong-field ionization in the relativistic regime.

[1] D. Strickland and G. Mourou, Opt. Commun. **56**, 219 (1985).

[2] S.-W. Bahk, P. Rousseau, T. A. Planchon, V. Chvykov, G. Kalintchenko, A. Maksimchuk, G. A. Mourou, and V. Yanovksy, Opt. Lett. **29**, 2837 (2004).

[3] A. D. DiChiara, I. Ghebregziabher, R. Sauer, J. Waesche, S. Palaniyappan, B. L. Wen, and B. C. Walker, Phys. Rev. Lett. **101**, 173002 (2008); S. Palaniyappan, R. Mitchell, R. Sauer, I. Ghebregziabher, S. L. White, M. F. Decamp, and B. C. Walker, *ibid.* **100**, 183001 (2008).

[4] S. X. Hu and C. H. Keitel, Phys. Rev. A **63**, 053402 (2001).

[5] L. N. Gaier and C. H. Keitel, Phys. Rev. A **65**, 023406 (2002).

[6] H. G. Hetzheim and C. H. Keitel, Phys. Rev. Lett. **102**, 083003 (2009).

[7] H. Bauke, H. G. Hetzheim, G. R. Mocken, M. Ruf, and C. H. Keitel, Phys. Rev. A **83**, 063414 (2011).

[8] L. V. Keldysh, Zh. Eksp. Teor. Fiz. **47**, 1945 (1964) [Sov. Phys. JETP **20**, 1307 (1965)]; F. H. M. Faisal, J. Phys. B **6**, L89 (1973); H. R. Reiss, Phys. Rev. A **22**, 1786 (1980).

[9] H. R. Reiss, Phys. Rev. A **42**, 1476 (1990).

[10] H. R. Reiss, J. Opt. Soc. Am. B **7**, 574 (1990).

[11] D. M. Wolkow, Z. Phys. **94**, 250 (1935).

[12] V. Popov, V. Mur, and B. Karnakov, JETP Lett. **66**, 229 (1997).

[13] V. Mur, B. Karnakov, and V. Popov, Zh. Eksp. Teor. Fiz. **114**, 798 (1998) [Sov. Phys. JETP **87**, 433 (1998)].

[14] N. Milosevic, V. P. Krainov, and T. Brabec, Phys. Rev. Lett. **89**, 193001 (2002); J. Phys. B **35**, 3515 (2002).

[15] J. I. Gersten and M. H. Mittleman, Phys. Rev. A **12**, 1840 (1975).

[16] V. P. Krainov, J. Opt. Soc. Am. B **14**, 425 (1997).

[17] S. V. Popruzhenko, G. G. Paulus, and D. Bauer, Phys. Rev. A **77**, 053409 (2008).

[18] L. Torlina and O. Smirnova, Phys. Rev. A **86**, 043408 (2012).

[19] C. J. Joachain, N. J. Kylstra, and R. M. Potvliege, J. Mod. Opt. **50**, 313 (2003).

[20] P. L. He, D. Lao, and F. He, Phys. Rev. Lett. **118**, 163203 (2017).

[21] M. Klaiber, E. Yakaboylu, and K. Z. Hatsagortsyan, Phys. Rev. A **87**, 023418 (2013); M. Klaiber, E. Yakaboylu, H. Bauke, K. Z. Hatsagortsyan, and C. H. Keitel, Phys. Rev. Lett. **110**, 153004 (2013).

[22] M. Klaiber, E. Yakaboylu, and K. Z. Hatsagortsyan, Phys. Rev. A **87**, 023417 (2013).

[23] M. Ferray, A. L'Huillier, X. F. Li, L. A. Lomprk, G. Mainfray, and C. Manus, J. Phys. B **21**, L31 (1988).

[24] T. Popmintchev, M. C. Chen, D. Popmintchev, P. Arpin, S. Brown, S. Ališauskas, G. Andriukaitis, T. Balčiunas, O. D. Mücke, A. Pugzlys *et al.*, Science **336**, 1287 (2012).

[25] T. Fan, P. Grychtol, R. Knut, C. Hernández-Garcia, D. D. Hickstein, D. Zusin, C. Gentry, F. J. Dollar, C. A. Mancuso, C. W. Hogle *et al.*, Proc. Natl. Acad. Sci. USA **112**, 14206 (2015).

[26] D. Popmintchev, C. Hernández-Garcia, F. Dollar, C. Mancuso, J. A. Pérez-Hernández, M. C. Chen, A. Hankla, X. H. Gao, B. Shim, A. L. Gaeta *et al.*, Science **350**, 1225 (2015).

[27] J. L. Krause, K. J. Schafer, and K. C. Kulander, Phys. Rev. Lett. **68**, 3535 (1992); Phys. Rev. A **45**, 4998 (1992).

[28] C. H. Keitel, P. L. Knight, and K. Burntt, Europhys. Lett. **24**, 539 (1993).

[29] C. H. Keitel and P. L. Knight, Phys. Rev. A **51**, 1420 (1995).

[30] M. W. Walser, C. H. Keitel, A. Scrinzi, and T. Brabec, Phys. Rev. Lett. **85**, 5082 (2000).

[31] D. B. Milošević, S. Hu, and W. Becker, Phys. Rev. A **63**, 011403(R) (2000).

[32] T. Baeva, S. Gordienko, and A. Pukhov, Phys. Rev. E **74**, 046404 (2006).

[33] C. C. Chirila, C. J. Joachain, N. J. Kylstra, and R. M. Potvliege, Phys. Rev. Lett. **93**, 243603 (2004).

[34] N. Milosevic, P. B. Corkum, and T. Brabec, Phys. Rev. Lett. **92**, 013002 (2004).

[35] M. Klaiber, K. Z. Hatsagortsyan, and C. H. Keitel, Phys. Rev. A **74**, 051803(R) (2006).

[36] R. Fischer, M. Lein, and C. H. Keitel, Phys. Rev. Lett. **97**, 143901 (2006).

[37] Q. Lin, S. Li, and W. Becker, Opt. Lett. **31**, 2163 (2006).

[38] M. Verschl, Laser Phys. **18**, 598 (2008).

[39] M. Kohler, T. Pfeifer, K. Hatsagortsyan, and C. Keitel, Adv. At., Mol. Opt. Phys., **61**, 159 (2012).

[40] M. Klaiber, K. Z. Hatsagortsyan, J. Wu, S. S. Luo, P. Grugan, and B. C. Walker, Phys. Rev. Lett. **118**, 093001 (2017).

[41] M. Li, J. W. Geng, M. Han, M. M. Liu, L. Y. Peng, Q. Gong, and Y. Liu, Phys. Rev. A **93**, 013402 (2016); M. Li, M.-M. Liu, J.-W. Geng, M. Han, X. Sun, Y. Shao, Y. Deng, C. Wu, L-Y. Peng, Q. Gong, and Y. Liu, *ibid.* **95**, 053425 (2017).

[42] P. B. Corkum, Phys. Rev. Lett. **71**, 1994 (1993).

[43] V. P. Krainov and B. Shokri, Laser Phys. **5**, 793 (1995).

[44] L. D. Laudau and E. M. Lifschitz, *Quantum Mechanics (Non-relativistic Theory)* (Oxford University Press, New York, 1958).

[45] Y. I. Salamin and C. H. Keitel, Phys. Rev. Lett. **88**, 095005 (2002).

[46] G. G. Paulus, W. Becker, W. Nicklicht, and H. Walther, J. Phys. B: At., Mol. Opt. Phys. **27**, L703 (1994).

[47] M.-M. Liu, M. Li, Y. Shao, M. Han, Q. Gong, and Y. Liu, Phys. Rev. A **96**, 043410 (2017).